Posted on 14 Sep 2024 — The copyright holder is the author/funder. All rights reserved. No reuse without permission. — https://doi.org/10.22541/au.172630278.80471242/v1 — This is a preprint and has not been peer-reviewed. Data may be preliminary.

Allosteric probe-driven catalytic CRISPR-Cas12a and dual-colored persistent luminescence nanoparticles tandem biosensing for ultra-sensitive MRSA detection

Shuai Liu[1], Zishan Ding[1], Zhiyong Liu[1], Yang Zhou[1], Xing Lu [1], Man Shen[1], Xianling Dai[1], Hanqing Xu[1], Jun Wang[1], Jing Bao[1], and Ming Chen[1]

[1]Third Military Medical University Southwest Hospital

September 14, 2024

Abstract

Methicillin-resistant Staphylococcus aureus (MRSA) is a prevalent and highly virulent bacterium encountered in clinical settings. Due to its uneven drug resistance profile and the multitude of factors influencing detection rates, precise and sensitive identification of MRSA is essential. Herein, we developed a detection system (called "APC-Cas-PLNPs") that can ultra-sensitive detection for MRSA, using nucleic acid-based allosteric probe, CRISPR-Cas12a and dual-colored persistent luminescent nanoparticles tandem detection. Simply, allosteric probe was used for specifically recognize MRSA and cyclic signal amplification, and then initiated catalytic CRISPR-Cas12a collateral cleavage. Meanwhile, red-emitting ZnGa2O4:Cr (ZGC) bonded with BHQ3 modified single-stranded DNA to create a detection probe known as ZGC@BHQ3, and green-emitting Zn2GeO4:Mn (ZGM) was utilized as the reference probe and electrostatically bound to both probes, forming the ratiometric luminescence sensor ZGC@BHQ3-ZGM for CRISPR-Cas12a detection.With this strategy, the non-nucleic acid targets were dexterously converted into fluorescent signals. This tandem detection system eliminates interference from background fluorescence and external factors, and provided a novel signal amplification and conversion strategy, which enables accurate and sensitive quantification of MRSA (1-105 CFU/mL) without requiring isolation and DNA extraction. Moreover, APC-Cas-PLNPs can recognize low levels of MRSA in food samples such as milk and orange juice, as well as in mouse serum, demonstrating greater sensitivity compared to real-time PCR. This method holds significant potential application value in food detection and early diagnosis of pathogenic bacteria, highlighting its broad applicability.

Allosteric probe-driven catalytic CRISPR-Cas12a and dual-colored persistent luminescence nanoparticles tandem biosensing for ultra-sensitive MRSA detection

Shuai Liu[1†], Zishan Ding[1†], Zhiyong Liu[1], Yang Zhou[1], Xing Lu[1], Man Shen[1], Xianling Dai[1], Hanqing Xu[1], Jun Wang[1]*, Jing Bao[1]*, Ming Chen[1,2,]*

[1]Department of Clinical Laboratory Medicine, Southwest Hospital, Third Military Medical University (Army Medical University), Chongqing 400038, P. R. China;

[2]College of Pharmacy and Laboratory Medicine, Third Military Medical University (Army Medical University), Chongqing 400038, China;

[†]Shuai Liu, Zishan Ding contributed equally to the writing of manuscript.

*Corresponding author. E-mail addresses: wangjun@tmmu.edu.cn (J. Wang), baojing_1991@tmmu.edu.cn (J. Bao), chenming1971@tmmu.edu.cn (M. Chen).

Abstract

Methicillin-resistant *Staphylococcus aureus* (MRSA) is a prevalent and highly virulent bacterium encountered in clinical settings. Due to its uneven drug resistance profile and the multitude of factors influencing detection rates, precise and sensitive identification of MRSA is essential. Herein, we developed a detection system (called "APC-Cas-PLNPs") that can ultra-sensitive detection for MRSA, using nucleic acid-based allosteric probe, CRISPR-Cas12a and dual-colored persistent luminescent nanoparticles tandem detection. Simply, allosteric probe was used for specifically recognize MRSA and cyclic signal amplification, and then initiated catalytic CRISPR-Cas12a collateral cleavage. Meanwhile, red-emitting $ZnGa_2O_4$:Cr (ZGC) bonded with BHQ3 modified single-stranded DNA to create a detection probe known as ZGC@BHQ3, and green-emitting Zn_2GeO_4:Mn (ZGM) was utilized as the reference probe and electrostatically bound to both probes, forming the ratiometric luminescence sensor ZGC@BHQ3-ZGM for CRISPR-Cas12a detection.With this strategy, the non-nucleic acid targets were dexterously converted into fluorescent signals. This tandem detection system eliminates interference from background fluorescence and external factors, and provided a novel signal amplification and conversion strategy, which enables accurate and sensitive quantification of MRSA (1-10^5 CFU/mL) without requiring isolation and DNA extraction. Moreover, APC-Cas-PLNPs can recognize low levels of MRSA in food samples such as milk and orange juice, as well as in mouse serum, demonstrating greater sensitivity compared to real-time PCR. This method holds significant potential application value in food detection and early diagnosis of

pathogenic bacteria, highlighting its broad applicability.

Keywords: Methicillin-resistant *Staphylococcus aureus* (MRSA); Allosteric probe; CRISPR-Cas12a; Ratiometric luminescence sensor; Tandem detection system

1 Introduction

Methicillin-resistant *Staphylococcus aureus* (MRSA) is a prevalent clinical antibiotic-resistant pathogen with robust pathogenicity and resistance to most antibiotics, making infection treatment challenging.[1,2] Therefore, the prompt and precise detection and identification of MRSA are crucial in curbing the spread of this pathogen. Conventional methods for MRSA detection include traditional bacterial isolation culture, amplification-based molecular diagnostic techniques and matrix assisted laser desorption ionization time of flight mass spectrometry (MALDI-TOF).[3-5] However, these approaches often entail intricate and time-consuming programs, limiting their suitability for swift and on-site monitoring of microbial contamination.[6] Particularly in the initial phases of pathogen infection, effectively quantifying low levels of pathogen poses a challenge. Hence, it is imperative to devise straightforward and cost-effective techniques for detecting minute traces of MRSA with high sensitivity and specificity, thereby facilitating targeted treatment options in clinical settings.

The CRISPR-Cas system, renowned for its swift and precise diagnostic capabilities in identifying and cleaving specific nucleic acid fragments,[7-9] has been harnessed alongside nucleic acid amplification modules to enable nucleic acid signal amplification detection. For example, researchers have pioneered isothermal amplification techniques, such as loop mediated isothermal amplification (LAMP),[10] recombinase polymerase amplification (RPA),[11] and nucleic acid sequence amplification (NASBA)[12] in combination with CRISPR-Cas system. This synergy not only enhances the sensitivity and specificity of CRISPR detection,[13, 14] but also obviates

the need for thermal cyclers typically required by PCR. Nevertheless, pathogens detection often necessitates prior nucleic acid extraction of the target before amplification, a process involving multiple enzymes that may lead to cross-contamination and non-specific amplification.[15, 16] Recent studies have highlighted that aptamer and non-nucleic acid targets exhibit remarkable affinity and specificity for recognition under enzyme-free conditions, thereby circumventing the need for nucleic acid extraction.[17, 18] Consequently, it can be deduced that by designing allosteric probe (AP) as binding units and utilizing allosteric DNA molecules to catalyze DNA reactions, linear signal amplification can be generated, achieving a one-pot reaction of amplification process and CRISPR-Cas reaction concurrently.

Researchers have commonly utilized the trans cleavage properties of Cas enzymes to convert detection signals into light signals.[19, 20] Traditional molecular beacons are obtained by connecting fluorescent groups with short nucleic acid chains and fluorescence-quenching groups, which have low luminosity, monochromatic emission, and small Stokes shift between excitation and emission peaks.[21] Therefore, experiments using such molecular beacons require highly sensitive optical equipment to readout, which in turn requires amplification of target nucleic acids to enhance Cas activity. [22, 23] In addition, the detection relying on a singular fluorescence signal is susceptible to variations in testing conditions, potentially resulting in the generation of false positive outcomes.[24] The ratiometric detection method, incorporating a reference signal, enables self-correction of fluorescence detection results and improves detection precision, thereby eliminating the influence of the aforementioned adverse factors.[25] Currently,

the majority of ratiometric luminescence sensors necessitate continuous external excitation light sources, making it challenging to circumvent interference within the sample matrix, consequently significantly affecting target detection accuracy.[26, 27]

Persistent luminescent nanoparticles (PLNPs), as an emerging photonic nanomaterial, exhibit unique persistent luminescent properties after the cease of excitation, surpassing traditional luminescent materials and eliminating autofluorescence interference in biosensing and biomedical imaging.[28, 29] Besides, the luminosity of PLNPs is several orders of magnitude higher than that of commonly used fluorescent groups such as 5-FAM (5-Carboxy fluorescein) and Cy3 (Sulfo-Cyanine3), with strong ultraviolet absorption and large emission offset, as well as special photostability.[30] Due to their unique optical properties, PLNPs are ideal energy donors for luminescence resonance energy transfer (LRET).[31] For example, Guo et al. developed a ratiometric aptasensor based on dual color PLNPs for precise detection of ochratoxin A. The sensor was not affected by real-time excitation and autofluorescence, with a detection limit as low as 3.4 pg mL^{-1}.[32] Similarly, Pan et al. also reported a PLNPs-based ratiometric sensor for detecting trace aflatoxin B1 in food samples.[33] Although the above methods eliminate the interference of autofluorescence by utilizing PLNPs-based ratiometric sensor, they do not combine the target amplification module with the sensor, which seriously reduces the sensitivity of detection. To improve the signal output, the target amplification module in tandem with the sensor module is highly desired. However, to the best of our knowledge, there have been no documented instances of utilizing AP to induce CRISPR-Cas12a coupled with a PLNPs-based

ratiometric luminescence sensor for the quantification of pathogens to achieve ultra-sensitive detection.

Herein, we designed and synthesized an AP initiated catalysis CRISPR-Cas12a collateral cleavage in tandem with a PLNPs-based dual-color ratiometric luminescence sensor ZGC@BHQ3-ZGM for pathogen detection, termed the "APC-Cas-PLNPs" system. This detection system provides a rapid, ultra-sensitive, and remarkably specific approach for direct pathogen detection, eliminating the need for strain isolation and nucleic acid extraction. Additionally, the capability of APC-Cas-PLNPs in detecting low-level MRSA in food samples like milk and orange juice, as well as in mouse serum, was validated in comparison with real-time PCR. The results of this research suggest that APC-Cas-PLNPs holds great potential for the detection of pathogenic bacteria in food safety and clinical diagnosis.

2 Materials and methods

In compliance with the word count restriction, this part has been put in supplementary information.

3 Results and discussion

3.1 Mechanism and fabrication of the APC-Cas-PLNPs

In the initial phase of our research (Fig. 1a), a distinctive allosteric probe (AP) was employed. This probe comprises a single-stranded DNA molecule with three distinct functional domains: the aptamer domain (blue) for MRSA recognition, the primer-binding site domain (green), and the stem sequence domain (red). The aptamer

developed by Turek et al. using Cell SELEX technology, to specifically recognize MRSA was selected as the DNA sequence of the AP aptamer domain, with a sequence length (75 nt) and dissociation constant (K_d = 1.6 ± 0.5 × 10^2 nmol/L).[34] To maintain the structural stability and prevent self-elongation, a phosphate group was introduced at the 3′ end of the AP, thereby increasing the resistance to enzymatic hydrolysis. In the absence of MRSA, the AP remains inactive, adopting a hairpin structure that conceals the primer-binding site domain, thereby hindering the downstream reactions. However, upon recognition and binding of MRSA by the aptamer domain of AP, the hairpin structure is destabilized, resulting in an active configuration that allows primer annealing and exposes the binding site domain. Subsequently, with the assistance of DNA polymerase, AP functions as a template for the production of double-stranded DNA (dsDNA), and releases MRSA for the next catalytic cycle, achieving signal amplification. In downstream reactions involving Cas12a-crRNA, the Wedge (WED) and PAM-interacting (PI) domains of Cas12a proteins recognize the protospacer adjacent motif (PAM) sequence of dsDNA targets, facilitating their unfolding.[35] The Cas12a-crRNA complex then binds to proximal dsDNA, initiating the trans-cleavage activity of Cas12a.

In the second section, we have crafted a dual-color ratiometric luminescence sensor. As depicted in Fig. 1b and Fig. 3a, cDNA-BHQ3 (a BHQ3-modified chain) modified ZGC with red-emitting (696 nm) ZGC (ZGC@BHQ3) was used as a detection signal. Meanwhile, green-emitting (533 nm) ZGM was methylated to prepare positively charged ZGM-$N^+(CH_3)_3$ as a reference signal. The ratiometric luminescence sensor,

ZGC@BHQ3-ZGM, was fabricated via the electrostatic interaction of the positively charged ZGM-$N^{+}(CH_3)_3$ with the negatively charged ZGC@BHQ3. When MRSA is recognized by the AP, Cas12a is activated, acquiring the capability to randomly cleave single chains and reinstating the red fluorescence signal of ZGC, whereas the fluorescence of ZGM remains unaltered. The entire sample-to-result process took approximately 55 min. Consequently, the ingenious APC-Cas-PLNPs system facilitates ultrasensitive and highly specific detection of MRSA, which eliminates the autofluorescence and external interference.

3.2 Analysis of AP performance

As illustrated in Fig. 2a, to affirm the specific binding of AP to MRSA and its subsequent transition to an active structure, we synthesized covalently modified AP, wherein the fluorescent group FAM is covalently attached to the 3′ end of primer-binding site domain, while the quenching group BHQ1 is covalently and internally linked to the 5′ end of the aptamer domain. The inverted fluorescence microscope image verifies that AP has been combined with MRSA and switched to the active structure (Fig. 2a). In addition, AP was mixed with different pathogenic bacteria for incubation to observe fluorescence images and fluorescence intensity (Fig. S1). Therefore, it can be considered that the constructed AP exhibited strong specificity for MRSA. To further validate that the combination of AP and MRSA triggered the amplification of dsDNA, the results of polyacrylamide gel electrophoresis (PAGE) analysis reveal that AP still maintained its original structure (Line3) when AP mixed solely with primer (Line2) or simultaneously with primer and Klenow Fragment (KF) DNA polymerase. However, in the presence of MRSA, AP underwent structural unfolding, and an extension reaction

upon co-incubation with the primer and KF DNA polymerase was triggered, which resulted in the generation of a substantial amount of dsDNA (Line4) (Fig. 2b). Moreover, the trans-cleavage activity of CRISPR-Cas12a was also confirmed. As illustrated in Fig. 2c, in the presence of target dsDNA, Cas12a exhibited robust activity under the guidance of crRNA.

To demonstrate the stability of AP in the absence of MRSA, the stem length in the AP structure was investigated. The variations in fluorescence intensity (△intensity) of AP to 6 different stem lengths (9, 10, 12, 14, 15 and 16 bp) were monitored (Fig. 2d). The △intensity decreases along with the stem length increase, regardless of the presence or absence of MRSA. However, as the stem length increased from 9 bp to 14 bp, a significant decrease in background signal and a slight decrease of signal resulted in an increase in the signal-to-background ratio (S/BG) (blue line), and then decreased obviously from 14 bp to 16 bp. Therefore, it can be inferred that the excessively long stem length leads to overly stable AP, hindering the unfolding of the AP structure, which is detrimental to subsequent dsDNA amplification and Cas12a activation. These observations align well with the computed Gibbs free energy (ΔG) and melting temperature (T_m) values of AP with different lengths of stem (Table S2). The aforementioned data underscores that the AP with a stem length of 14 bp (AP-14 stem) has excellent stability and state switching dynamics, which was chosen as the AP in the APC-Cas-PLNPs system.

3.3 Preparation and characterization of ratiometric luminescence sensor

The elaborate design and meticulous preparation of the innovative ratiometric luminescence sensor ZGC@BHQ3-ZGM are highlighted in Fig. 3a. The preparation of

positively charged ZGM-$N^+(CH_3)_3$ as a reference probe by methylation of ZGM. cDNA-BHQ3 was connected to ZGC surface to form ZGC@BHQ3 as the detection probe. ZGC@BHQ3-ZGM was finally obtained by combining positively charged ZGM-$N^+(CH_3)_3$ with negatively charged ZGC@BHQ3 via electrostatic interaction. As depicted in Fig. 3b, TEM image reveals that the ZGM display a typical rod-like morphology, with a length between 40-75 nm. HR-TEM reveals that the synthesized ZGM has high crystallinity, and the distance between the two adjacent lattice fringes is 0.29 nm, which is corresponding to the distance between the (113) lattice planes. Additionally, the power X-ray diffraction (XRD) results provide unequivocal evidence that ZGM adopts a pristine diamond-like crystal structure of Zn_2GeO_4 (Fig. S2), demonstrating its pristine purity and crystallinity. Moreover, high-angle annular dark-field scanning TEM (HAADF) imaging and energy dispersive spectroscopy (EDS) (Fig. S3a) confirmed the presence of Zn, Ge, Mn and O elements in the structures of ZGM. In order to bind the ZGC, the ZGM are functionalized with amino group, then the nanorods were further reacted with CH_3I to obtain ZGM-$N^+(CH_3)_3$. FT-IR spectra showed that the characteristic peaks of ZGM-$N^+(CH_3)_3$ at 3433 cm^{-1}, 2927-2855 cm^{-1}, 1197 cm^{-1} and 1076 cm^{-1} are ascribed to the stretching vibration of -NH_2, -CH_2-, C-N and -Si-O-Si-, respectively, indicating the -$N^+(CH_3)_3$ group was successful modified on the surface of the ZGM (Fig. S4a). Moreover, after the modification, the hydrodynamic size of ZGM-$N^+(CH_3)_3$ increased significantly (Fig. 3e), and the zeta potential changed from -33.2 ± 3.2 mV to 32.9 ± 2.8 mV (Fig. 3g), both of which serve as definitive indicators of the successful preparation of ZGM-$N^+(CH_3)_3$.

Meanwhile, the ZGC were synthesized by doping the Cr^{3+} into the matrix $ZnGa_2O_4$ via hydrothermal method. Fig. 3c and Fig. S2 shows that the ZGC are granular with the diameters in the range of 5-9 nm, and the ZGC have the standard rhombic crystal structure of $ZnGa_2O_4$, with a distance of 0.25 nm between two neighboring lattice planes, which corresponds to the distance between the (311) lattice planes. In addition, HAADF imaging and EDS (Fig. S3b) confirmed the presence of the elements Zn, Ga, Cr and O in the ZGC. In order to conjugate the cDNA-BHQ3, the ZGC was functionalized amino groups. The characteristic peaks of ZGC-NH_2 at 3424 cm^{-1}, 2928-2853 cm^{-1} and 1062 cm^{-1} belonged to the stretching vibration of -NH_2, -CH_2- and -Si-O-Si-, confirming the successful modification of -NH_2 (Fig. S4b). Also, the hydrodynamic size of ZGC-NH_2 increased compared to ZGC (Fig. 3f) and the zeta potential changed from 23.7 ± 2.5 mV to 35.0 ± 3.4 mV (Fig. 3h). Thus, it can be considered that ZGC-NH_2 was successfully prepared.

Next, to prepare the ratiometric luminescence sensor, we first prepared ZGC@BHQ3 to quench the red fluorescence of ZGC by utilizing the amino and thiol groups reaction between ZGC-NH_2 and cDNA-BHQ3 (5′-SH-TATATATCGATGCGCCATCG-BHQ3-3′). As shown in Fig. 3f, the hydrodynamic size of ZGC@BHQ3 had slightly increased compared to ZGC-NH_2. Meanwhile, the zeta potential changed from 35.0 ± 2.2 mV to -17.1 ± 1.6 mV, which was attributed to the introduction of a phosphate group in the cDNA-BHQ3 (Fig. 3h). These findings unequivocally indicate the successful preparation of ZGC@BHQ3. Subsequently, the positively charged ZGM-$N^+(CH_3)_3$ was combined with the negatively charged

ZGC@BHQ3 via electrostatic interaction to obtain the ratiometric luminescence sensor ZGC@BHQ3-ZGM. The hydrodynamic size of ZGC@BHQ3-ZGM increased to 712.4 ± 40.2 nm (Fig. 3f) and the zeta potential changed to 15.8 ± 1.1 mV (Fig. 3h). TEM images revealed a distinct core-shell architecture in the prepared ZGC@BHQ3-ZGM, characterized by a granular ZGC shell adsorbed on a rod-shaped ZGM core (Fig. 3d, white box). The results of HAADF images and EDS indicate the presence of Zn, Ge, Mn, Ga, Cr, and O elements in ZGC@BHQ3-ZGM. Due to the extremely low content of Mn and Cr in the structure of ZGM and ZMC, the element mapping is not significant. It is noteworthy that Ga was conspicuously present in ZGC (white box), absent in ZGM, while Ge, on the other hand, was detected in ZGM but not in the designated area of ZGC. Additionally, the XRD results indicate that ZGC@BHQ3-ZGM has a high crystallinity with diffraction peaks originating from $ZnGa_2O_4$ and Zn_2GeO_4 (Fig. S2). Collectively, these findings conclusively validate the successful preparation of the ratiometric luminescence sensor, with ZMG and ZGC retaining their inherent morphology and crystalline structure.

3.4 Analysis of ZGC@BHQ3-ZGM performance

To assess the performance of the ratiometric luminescence sensor ZGC@BHQ3-ZGM, the optical properties of ZGM and ZGC were initially investigated. As depicted in Fig. 4a and b, upon excitation with UV light at 254 nm, ZGM and ZGC exhibited emissions in green and red luminescence at 533 nm and 696 nm, respectively. These typical near infrared emissions were originated from $^4T_1$ (4G)-^{6}A1 (6S) transition of doped Mn^{2+} and $^2E \rightarrow {}^4A_2$ transitions of twisted Cr^{3+}.[36,37] To prove the successful

bioconjugation between ZGC and BHQ3, UV–vis absorption of BHQ3, and emission spectra of ZGC and ZGC@BHQ3 were measured, respectively. As shown in Fig. 4c, the quenching rate of BHQ3 on ZGC was determined to be 88.3%, which was due to the shortened distance between ZGC and BHQ3, resulting in effective energy transfer. This result offered a minimal background signal for MRSA detection. Besides, ZGM and ZGC have long-lasting afterglow after UV lamp irradiation (254 nm, 5 min), confirming that the prepared ZGC@BHQ3-ZGM has excellent afterglow performance (Fig. 4d).

Furthermore, to ascertain the potential impact of single-emissive PLNPs on ZGC@BHQ3-ZGM (Fig. 4e), an exploration into the influence of varying concentrations, test voltages, and durations on fluorescence intensity and fluorescence ratio at 537 nm and 696 nm (I_{696}/I_{533}) were investigated. Although the fluorescence intensity of each emission peak gradually increased along with the increase of ZGC@BHQ3-ZGM concentration and test voltage, I_{696}/I_{533} remained stable (Fig. 4f and g, Fig. S5a and b). Notably, Fig. 4h, Fig. S5c illustrates the fluorescence intensity at 533 nm and 696 nm rapidly decays with time, but the ratio of fluorescence intensity (I_{696}/I_{533}) remains almost unchanged, avoiding the influence of test time on the ZGC@BHQ3-ZGM. In addition, as the storage time changes, the fluorescence intensity and corresponding fluorescence ratio at 535 nm and 696 nm still kept constant, indicating that the ZGC@BHQ3-ZGM shows excellent stability (Fig. 4i, Fig. S5d). The abovementioned results collectively suggest that the developed ratiometric sensor boasts attributes such as immunity to autofluorescence interference, ease of

preservation, and significant practical utility.

3.5 Optimization of the experimental parameters

To enhance the efficiency of our experiments, we meticulously fine-tuned the detection conditions. The concentration of AP has a significant impact on the specific recognition of MRSA. The increase of the concentration of AP can increase the catalytic reaction rate and generate a large quantity of dsDNA (containing PAM sites) to activate more Cas12a in APC-Cas-PLNPs. Therefore, we first mixed MRSA (about 10^2 CFU/mL) with the AP to investigate the influence of AP concentration on the change of fluorescence intensity ratio ($\triangle(I_{696}/I_{533})$). As shown in Fig. S6a and S7a, $\triangle(I_{696}/I_{533})$ gradually increased with an increase in AP concentration from 100 to 400 nm. However, with a further increase in AP concentration to 500 nm, the $\triangle(I_{696}/I_{533})$ was significantly decreased. This may be due to the formation of dimers structures at excessively high AP concentration, which affect the binding efficiency of AP to MRSA. Consequently, we opted for a concentration of 400 nM for subsequent experiments. Furthermore, our investigation highlighted the pivotal role of DNA polymerase in dsDNA synthesis. It could be seen that the $\triangle(I_{696}/I_{533})$ increased with the increasing concentration of DNA polymerase and reached its maximum value at 0.05 U/μL (Fig. S6b and Fig. S7b). Thus, a concentration of 0.05 U/μL was deemed optimal for our future experiments. In addition, the concentration of crRNA was a critical factor for CRISPR/Cas12a-based signal amplification. Fig. S6c and Fig. S7c illustrate the concentration of crRNA ranged from 5 to 25 nM, and the $\triangle(I_{696}/I_{533})$ reached the maximum value at 20 nM. Lastly, we optimized the reaction time of the CRISPR/Cas12a system for trans cleavage. As shown

in Fig. S6d and Fig. S7d, $\triangle(I_{696}/I_{533})$ progressively increases from 5 to 15 min, and as time further increases to 20 to 25 min, the $\triangle(I_{696}/I_{533})$ shows no significant change. Therefore, the concentrations of APS, DNA polymerase and crRNA of 400 nM, 0.05 U/μL, and 20 nM, respectively, and the reaction time of 15 min were selected as the optimal conditions for MRSA detection.

3.6 APC-Cas-PLNPs for MRSA detection

To demonstrate the exceptional sensitivity of APC-Cas-PLNPs in detecting MRSA, a series of samples containing MRSA cells (1-10^6 CFU/mL) were prepared. The results in Fig.5a shown that $\triangle(I_{696}/I_{533})$ varied linearly with the amount of MRSA in the range of 1 to 10^5 CFU/mL, and APC-Cas-PLNPs can easily detect MRSA at levels as low as 1 CFU/mL. In comparison to alternative detection techniques, this assay system is distinguished by its capability to sustain a broader detection range and achieve a lower detection limit within a significantly shorter timeframe (Table S3). It can be inferred that the aptamer domain of AP demonstrates exceptional MRSA specific recognition ability, leading to the disruption of the secondary structure of AP upon MRSA recognition. Subsequently, under the action of DNA polymerase, dsDNA containing PAM site is synthesized, allowing MRSA to proceed into the next catalytic cycle, thereby achieving primary amplification. In addition, the prepared dual-color ratiometric luminescence sensor ZGC@BHQ3-ZGM possesses significant advantages such as strong ultraviolet absorption, large emission offset, high luminosity, eliminating autofluorescence interference, and high signal/noise ratio. When the aforementioned dsDNA hybridizes with Cas12a/crRNA, it activates the collateral cleavage ability of

Cas12a, cleaving multiple ZGC@BHQ3 (secondary amplification), consequently generating amplified ratio fluorescence signals. The results obtained demonstrate that APC-Cas-PLNPs can detect a single MRSA through the two-stage amplification of the AP, CRISPR-Cas12a and dual-colored persistent luminescent nanoparticles tandem detection. Currently, real-time PCR is the most effective method for analyzing and quantifying pathogen due to its high sensitivity. Therefore, we compared APC-Cas-PLNPs system with real-time PCR for MRSA detection. The extracted genomic DNA of MRSA was within the range of 6×10-6×10^7 CFU/mL (genomic DNA range: 0.25-1.2×10^5 pg/μL) and subjected to real-time PCR reaction. As illustrated in Fig. 5b, the C_t value varies linearly within the range of 6×10^2-6×10^7 CFU/mL. However, when the amount of MRSA was below 6×10^2 CFU/mL, the C_t value is greater than 35. Even after more 40 cycles, 60 CFU/mL bacterial cells still have no C_t value. This disparity can be attributed to the loss of target sequences during genome extraction, underscoring the superior sensitivity and efficiency of the APC-Cas-PLNPs system over real-time PCR for MRSA detection.

The study further investigated the specificity of the APC-Cas-PLNPs system for detecting MRSA. Fig. 5c illustrates that in the presence of *K. pneumoniae*, *P. aeruginosa*, *E. coli* or *L. monocytogenes*, the fluorescence signal can be ignored; however, the $\triangle(I_{696}/I_{533})$ of MRSA was significantly increased than these pathogens ($P < 0.001$). In addition, we detected two methicillin-susceptible *S. aureus* (ATCC29213 and ATCC25923), and the results showed that APC-Cas-PLNPs could accurately distinguish MRSA from methicillin-susceptible *S. aureus* strains ($P < 0.001$) (Fig. 5d).

Therefore, it can be deduced that the developed APC-Cas-PLNPs system had excellent specificity for MRSA. Also, to further analyze the specificity of APC-Cas-PLNPs in complex samples, a mixture of MRSA and other pathogens was tested in a molar ratio of 1:10. As shown in Fig. 5e and f, whether mixed with pathogenic bacteria of different genera or *S. aureus* (ATCC29213 and ATCC25923), there is no significant difference in $\triangle(I_{696}/I_{533})$ compared to the presence of MRSA alone. In conclusion, these results emphasize the outstanding sensitivity and specificity of APC-Cas-PLNPs in MRSA detection, positioning it as a promising novel platform for pathogen identification.

3.7 Method validation and application to milk, orange juice and serum

To demonstrate the feasibility of proposed detection method in food sample detection, we evaluated the MRSA levels of pasteurized milk (PM) samples (n = 20) and contaminated milk (CM) samples (n = 20), as well as pasteurized orange juice (PO) samples (n = 20) and contaminated orange juice (CO) samples (n = 20) using APC-Cas-PLNPs in a blind validation study. As illustrated in Fig. 6a and d, all 20 contaminated milk or orange juice samples exhibited higher levels of $\triangle(I_{696}/I_{533})$ compared to pasteurized milk or orange juice samples, demonstrating that APC-Cas-PLNPs could effectively distinguish contaminated food samples from pasteurized food samples (P<0.001). However, C_t value showed that although there was a significant difference in the genomic DNA expression of MRSA between pasteurized milk or orange juice samples and contaminated milk or orange juice samples (P<0.01), there was a certain proportion of signal overlap between these two columns of data (Fig. 6b and e). The ROC curve of APC-Cas-PLNPs shows that compared to pasteurized milk samples, the

AUC values of contaminated milk or orange juice samples are both 1.0. By contrast, real-time PCR has a poorer classification of contaminated food samples from pasteurized food samples (AUC values of 0.85 and 0.77, respectively) (Fig. 6c and f). It can be considered that during the process of genome extraction, both target and non-target strains will be cleaved together, especially mixing trace amounts of MRSA genomic DNA with non-target strain genes will affect the concentration of detected nucleic acid sequences, leading to a decrease in real-time PCR sensitivity. Furthermore, the complexity of the amplification program and the specificity of primers can also affect the detection results. On the contrary, the APC-Cas-PLNPs detection system we established does not require genomic DNA extraction. Upon APS binding specifically to MRSA, the allosteric switch structure of AP would activate the collateral cleavage of CRISPR-Cas12a, while a ratiometric luminescence sensor using PLNPs as molecular beacons enables more sensitive and precise signal detection.

Finally, we infected 6-8-week-old mice with MRSA bacterial solution via intravenous injection, and used uninfected mice of the same age and number as control. Then, blood samples were collected, and the APC-Cas-PLNPs was used to detect MRSA in the mice serum (Fig. 6g). The $\triangle(I_{696}/I_{533})$ value of each mouse was detected by APC-Cas-PLNPs every 30 min for the first 6 h after infection, and then every 12 h until the 4^{th} d to prove the presence of MRSA in the mouse (Fig. 6h). As a result, the $\triangle(I_{696}/I_{533})$ value of the infected mice model increased over time, while there was no significant change in the $\triangle(I_{696}/I_{533})$ value of the uninfected mice, indicating that MRSA had already colonized and grown in the blood. It is worth noting that the

△(I_{696}/I_{533}) value of infected mice slightly decreased from 2.5 to 4 h, which may be due to the immune system clearing a portion of MRSA. The ROC curve of APC-Cas-PLNPs indicated an AUC of 0.98 in uninfected mice compared to infected mice, suggesting it has the potential to detect early MRSA infection (Fig. 6i). These above results fully demonstrate that the developed APC-Cas-PLNPs system is capable of the accurate detection of MRSA in food detection and clinical testing.

Author Contributions

J.W., J.B., and M.C. conceived, directed, and supervised the study and critically revised and approved the manuscript. S.L. and Z.D. performed the experiment, analyzed the data, and wrote the manuscript. Z.L., Y.Z., X.L., M.S., X.D., and H.X participated in the experiments and analyzed the data. All authors read and approved the final manuscript.

Acknowledgements

This work was supported by the National Key R&D Program of China (2022YFC2603800), the National Natural Science Foundation of China (82472385 and 82372105), the Chongqing Natural Science Foundation (CSTB2022NSCQ-MSX0151 and CSTB2022NSCQ-MSX0205), the Army Military Medical University Southwest Hospital Doctor Youth Lift project 2024BQTJ-3.

Conflict of Interest Statement

The authors declare no conflict of interest.

418

419 **ORCID**

420 Ming Chen https://orcid.org/0000-0003-0613-7932

421

422 **Abbreviations**

423 MRSA, Methicillin-resistant *Staphylococcus aureus*; AP, allosteric probe; PLNPs,
424 persistent luminescent nanoparticles; APC-Cas-PLNPs, allosteric probe initiated
425 catalysis CRISPR-Cas12a collateral cleavage in tandem with a dual-color PLNPs-based
426 ratiometric luminescence sensor ZGC@BHQ3-ZGM for pathogen detection; TEM,
427 transmission electron microscopy; HR-TEM, high resolution-transmission electron
428 microscopy; XRD, X-ray diffraction; FT-IR, fourier transform infrared; HAADF, high-
429 angle annular dark-field scanning TEM; EDS, energy dispersive spectroscopy; PM,
430 pasteurized milk; CM, contaminated milk; PO, pasteurized orange juice; CO,
431 contaminated orange juice.

432

433 **References**

434 1. Y. Cong, S. Yang, X. Rao, *J. Adv. Res.* ***2019***, *21*:169-176. doi:
435 https://doi.org/10.1016/j.jare.2019.10.005.
436 2. Q.Q. He, J. Meneely, I.R. Grant, J. Chin, S. Fanning, C. Situ, *Chin. Med.* ***2024***,
437 *19*, 1. doi: https://doi.org/10.1186/s13020-024-00960-8.
438 3. B. Baumann, A. Martin, B. Malorny, Int. J. Food. Microbiol. ***2015***, *193*:8-14.
439 doi: https://doi.org/ 10.1016/j.ijfoodmicro.2014.10.004.
440 4. R.W. Li, J.T. Yan, B. Feng, M. Sun, C.F. Ding, H. Shen, J. Zhu, S. Yu, *ACS*

Appl. Mater. Interfaces. ***2023***, *15*:18663-18671. doi: https://doi.org/10.1021/acsami.3c00632.

5. L.Váradi, J.L. Luo, D.E. Hibbs, J.D. Perry, R.J. Anderson, S. Orenga, P.W. Groundwater, *Chem. Soc. Rev.* ***2017***, *46*(16):4818-4832. doi: https://doi.org/10.1039/c6cs00693k.

6. M.M. Hassan, A. Ranzoni, M.A. Cooper, *Biosens. Bioelectron.* ***2018***, *99*:150-155. doi: https://doi.org/10.1021/acsami.3c00632.

7. J.F.K. Elliott, D. McLeod, T.B. Taylor, E.R. Westra, S. Gandon, B.N.J. Watson, *ISME*. *J* ***2024***, 18(1). doi: https://doi.org/10.1093/ismejo/wrae108.

8. J. G. Zalatan, M. E. Lee, R, Almeida. L. A. Gilbert, E. H. Whitehead, M. La Russa, C. T. Jordan, S. W. Jonathan, E. D. John, S. Q. Lei, *Cell*, ***2015***, *160*(1-2):339-350. doi: https://doi.org/10.1016/j.cell.2014.11.052.

9. Z. Wang, W. Cui, *View*, ***2020***, *20200008*. doi: https://doi.org/10.1002/VIW.20200008

10. T. Notomi, H. Okayama, H. Masubuchi, T. Yonekawa, K. Watanabe, N. Amino, H. Tetsu, *Nucleic Acids. Res. 2000*, *28*(12):E63. doi: https://doi.org/10.1093/nar/28.12.e63.

11. R. K. Daher, G. Stewart, M. Boissinot, M. G. Bergeron, *Clin. Chem.* ***2016***, *62*(7):947-958. doi: https://doi.org/10.1373/clinchem.2015.245829.

12. K. Karasawa, H. Arakawa, *Luminescence* ***2022***, *37*(5):822-827. doi: https://doi.org/10.1002/bio.4226. doi: https://doi.org/10.1002/bio.4226.

13. M. Patchsung, K. Jantarug, A. Pattama, K. Aphicho, S. Suraritdechachai, P.

463 Meesawat, *Nat. Biomed. Eng.* ***2020***, *4*(12):1140-1149. doi:
464 https://doi.org/10.1038/s41551-020-00603-x.
465 14. S. Y. Lee, S. W. Oh, *Talanta* ***2022***, *241*:123186. doi: https://doi.org/241.
466 10.1016/j.talanta.2021.123186.
467 15. M. Aladhadh, *Microorganisms* ***2023***, 11(5):1111. doi:
468 https://doi.org/10.3390/microorganisms11051111.
469 16. S. Rao, *J. Hosp. Infect.* ***2006***, *64*:20-21. doi: https://doi.org/10.1016/S0195-
470 6701(06)60066-2.
471 17. A. Aihaiti, J. K. Wang, W. R. Zhang, M. P. Shen, F. X. Meng, Z. D. Li, *Compr.*
472 *Rev. Food. Sci Food Saf.* ***2024***, *23*(4):13358. doi: https://doi.org/10.1111/1541-
473 4337.13358.
474 18. J. Shen, X. M. Zhou, Y. Y. Shan, H. H. Yue, R. Huang, J. M. Hu, *Nat. Commun.*
475 ***2020***, *11*(1):267. doi: https://doi.org/10.1038/s41467-019-14135-9.
476 19. J. E. van Dongen, J. T. W. Berendsen, R. D. M. Steenbergen, R. M. F. Wolthuis,
477 J. C. T. LI Eijkel Segerink, *Biosens. Bioelectron.* ***2020***, *166*:112445. doi:
478 https://doi.org/10.1016/j.bios.2020.112445.
479 20. H. Li, M. L. Li, Y. C. Yang, F. Wang, C. Li. *Anal. Chem* ***2021***, *93*(6):3209-
480 3216. doi: https://doi.org/10.1021/acs.analchem.0c04687.
481 21. C. P. Liang, P. Q. Ma, H. Liu, X. G. Guo, B. C. Yin, B. C. Ye, *Angew. Chem. Int.*
482 *Edit.* ***2017***, *56*(31):9077-9081. doi: https://doi.org/10.1002/anie.201704147.
483 22. C. Van Tricht, T. Voet, J. Lammertyn, D. Spasic. *Trends Biotechnol.* ***2023***,
484 *41*(6):769-784. doi: https://doi.org/10.1016/j.tibtech.2022.10.003.

23. Y. X. Li, Z. W. Luo, C. Y. Zhang, R. Sun, C. Zhou, C. J. Sun, *Trends Anal. Chem.* ***2021***, *134*:116142. doi: https://doi.org/10.1016/j.trac.2020.116142.

24. D. E. Armstrong-Price, P. S. Deore, R. A. Manderville, J. Agric. *Food Chem.* ***2020***, *68*(7):2249-2255. doi: https://doi.org/10.1021/acs.jafc.9b07391.

25. L. M. Yang, X. H. Yin, B. An, F. Li, *Anal. Chem.* ***2021***, *93*(3):1709-1716. doi: https://doi.org/10.1021/acs.analchem.0c04308.

26. B. C. Su, Z. Zhang, Z. C. Sun, Z. W. Tang, X. X. Xie, Q. Chen, *J. Hazard Mater.* ***2022***, *422*:126838. doi: https://doi.org/10.1016/j.jhazmat.2021.126838.

27. Y. X. Yu, G. L. Li, *J. Hazard Mater.* ***2022***, *422*:126927. doi: https://doi.org/10.1016/j.jhazmat.2021.126927.

28. M. H. Chan, Y. C. Chang, *Anal. Bioanal. Chem.* ***2024***, *416*(17):3887-3905. doi: https://doi.org/10.1007/s00216-024-05267-z.

29. R. M. Calderón-Olvera, E. Arroyo, A. M. Jankelow, R. Bashir, E. M. Valera, *ACS Appl. Mater. Interfaces* ***2023***, *15*(17):20613-20624. doi: https://doi.org/10.1021/acsami.2c21735.

30. K. Ge, J. M. Liu, P. H. Wang, G. Z. Fang, D. D. Zhang, S. Wang, *Microchim Acta* ***2019***, *186*(3):197. doi: https://doi.org/10.1007/s00604-019-3294-z.

31. N. Le, J. S. Wang, L. Huang, L. Zeng, W. C. Xu, Z. J. Li, *Adv. Mater.* ***2022***, *34*(14):2107962. doi: https://doi.org/10.1002/adma.202107962.

32. J. X. Guo, L. M. Pan, M. C. Wang, L. J. Chen, X. Zhao, *Food Chem.* ***2023***, *413*:135611. doi: https://doi.org/10.1016/j.foodchem.2023.135611.

33. L. M. Pan, X. Zhao, X. Wei, L. J. Chen, C. Wang, X. P. Yan, *Anal. Chem.*

2022, *94*(16):6387-6393. doi: https://doi.org/10.1021/acs.analchem.2c00861.

34. M. X. X. Ran, R. Sun, J. Q. Yan, A. T. Pulliainen, Y. Zhang, H. B. Zhang, *Small* ***2023***, *19*(47). doi: https://doi.org/10.1002/smll.202304194.

35. H. Hirano, J. S. Gootenberg, T. Horii, O. O. Abudayyeh, M. Kimura, P. D. Hsu, *Cell*, ***2016***, *164*(5):950-961. doi: https://doi.org/10.1016/j.cell.2016.01.039.

36. Y. Q. Wang, Z. H. Li, Q. S. Lin, Y. R. Wei, J. Wang, Y. X. Li, *ACS Sens.* ***2019***, *4*(8):2124-2130. doi: https://doi.org/10.1021/acssensors.9b00927.

37. X. H. Wang, Y. H. Wang, S. Chen, P. Fu, Y. B. Lin, S. Y. Ye, *Biosens. Bioelectron* ***2022***, *198*:113849. doi: https://doi.org/10.1016/j.bios.2021.113849.

Figures

Fig. 1 Illustration of allosteric probe to initiate catalytic CRISPR-Cas12a collateral cleavage in tandem with dual-color ratiometric luminescence sensor ZGC@BHQ3-ZGM (APC-Cas-PLNPs) system for MRSA detection.

Fig. 2 Performance analysis of AP. (a) Illustration and representative inverted fluorescence microscope images of FAM/BHQ1-labeled AP binding to MRSA. (b) Feasibility of electrophoretic analysis for AP detection of MRSA. M: DNA ladder, Lane1: AP; Lane2: AP + primer; Lane 3: AP + primer + DNA polymerase; Lane4: AP + primer + DNA polymerase + MRSA. '+' means presence, '-' means absence. (c) Fluorescence intensity detection of CRISPR-Cas12a system. (d) Comparison of relative fluorescence intensity and signal-to-background ratio of AP with six different stem lengths. Values are the mean ± SD of the results from three independent experiment.

Fig. 3 The preparation process and characterization of ratiometric luminescence sensor ZGC@BHQ3-ZGM. (a) Schematic of the developed ratiometric luminescence sensor ZGC@BHQ_3-ZGM. (b) TEM, HR-TEM and element mapping images, and size distribution of ZGM. (c) TEM, HR-TEM and element mapping images, and size distribution of ZGC. (d) TEM, HR-TEM and element mapping images of ZGC@BHQ3-ZGM. The white box represents the TEM and element mapping images of ZGC. (e) Hydrodynamic size of ZGM, ZGM-NH_2 and ZGC-$N^+(CH_3)_3$. (f) Hydrodynamic size of ZGC, ZGC-NH_2, ZGC@BHQ3 and ZGC@BHQ3-ZGM. (g) Zeta potential of ZGM, ZGM-NH_2 and ZGC-$N^+(CH_3)_3$. (h) Zeta potential of ZGC, ZGC-NH_2, ZGC@BHQ3 and ZGC@BHQ3-ZGM.

Fig. 4 Performance analysis of ZGC@BHQ3-ZGM. Emission (excitation at 254 nm) spectra of ZGM, and the inset image refers to ZGM aqueous solution (0.5 mg/mL) (a). Emission (excitation at 254 nm) spectra of ZGC, and the inset image refers to ZGC aqueous solution (0.5 mg/mL) (b). Emission (excitation at 254 nm) spectra of ZGC@BHQ3, and the inset image refers to ZGC and ZGC@BHQ3 aqueous solution (0.5 mg/mL) (c). Afterglow decay curves of ZGM and ZGC (d). Emission spectrum (excitation at 254 nm) of ZGC@BHQ3-ZGM (e). Effects of ZGC@BHQ3-ZGM concentration (10-30 μg/mL) (f), test voltage (600-700 V) (g), test time (0-10 min) (h) and storage time (0-60 d) (i) on the fluorescence intensity and fluorescence ratio at 537 nm and 696 nm (I_{696}/I_{533}).

Fig. 5 Evaluation of APC-Cas-PLNPs system sensitivity and specificity for MRSA detection. (a) The fluorescence intensity of APC-Cas-PLNPs for detection of MRSA (The amount of MRSA from 1 to 10^6 CFU; insets: the linear analysis of MRSA detection by APC-Cas-PLNPs). (b) The C_t values of real-time PCR for detection of MRSA (The amount of MRSA from 6×10^2-6×10^7 CFU; insets: the linear analysis of MRSA detection by real-time PCR). (c-d) Specificity of APC-Cas-PLNPs for detection of MRSA (MRSA: 10^2 CFU/mL, all other pathogens: 10^3 CFU/mL). (e-f) Specificity of APC-Cas-PLNPs for MRSA detection in complex samples (the amount of MRSA was one-tenth of other pathogens). Values are the mean ± SD of the results from three independent experiments. Asterisks indicate significant differences (***, $P < 0.001$, by Student's *t* test).

Fig. 6 Measurement of MRSA in food samples and mouse serum. (a) $\triangle(I_{696}/I_{533})$ of

MRSA expressed in a milk blind validation cohort. PM: pasteurized milk; CM: contaminated milk; PO: pasteurized orange juice; CO: contaminated orange juice. (b) C_t value of the genomic DNA of MRSA in a milk blind validation cohort. (c) ROC curve analysis of blind validation queue for milk. (d) $\triangle(I_{696}/I_{533})$ of MRSA expressed in an orange juice blind validation cohort. (e) C_t value of the genomic DNA of MRSA in an orange juice blind validation cohort. (f) ROC curve analysis of blind validation queue for orange juice. (g) Construction of MRSA infected mouse model and schematic diagram of blood collection. (h) Growth curves of MRSA in infected and uninfected mice over time. The blue dashed line and the red dashed line represent the $\triangle(I_{696}/I_{533})$ of 6 infected mice and 6 uninfected mice over time, respectively. The blue solid line and the red solid line represent the average $\triangle(I_{696}/I_{533})$ of 6 infected and 6 uninfected mice over time, respectively. (i) ROC curve analysis of 6 uninfected mice versus 6 MRSA infected mice at all stage (0 to 96 h). Asterisks indicate significant differences (**, $P < 0.01$, ***, $P < 0.001$, by Student's *t* test).

574 Figure 1

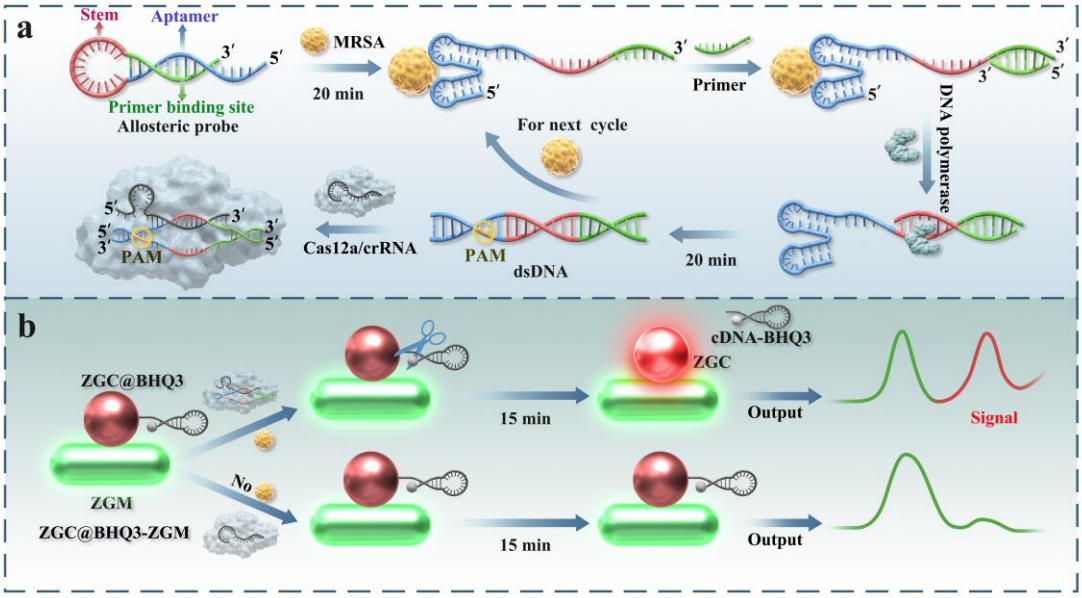

575

576

577 Figure 2

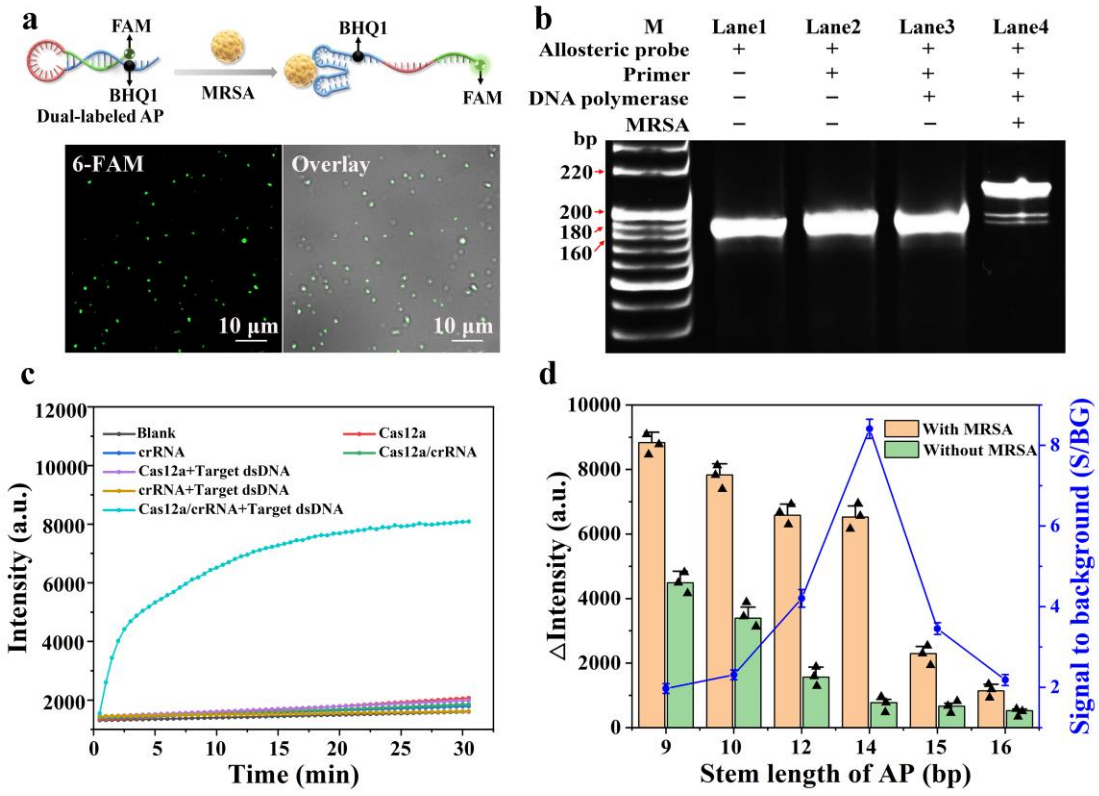

578

579 Figure 3

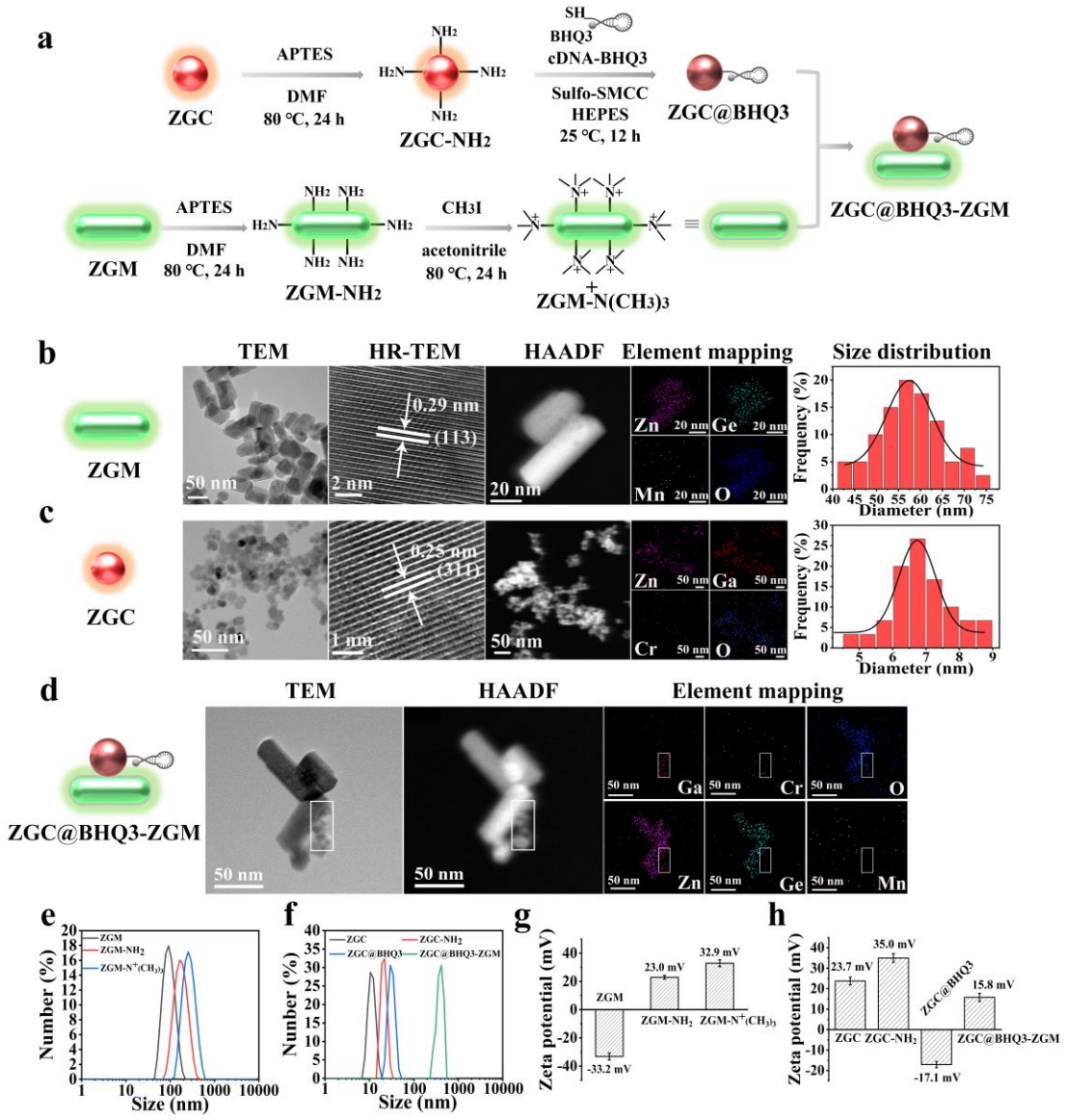

580

581 Figure 4

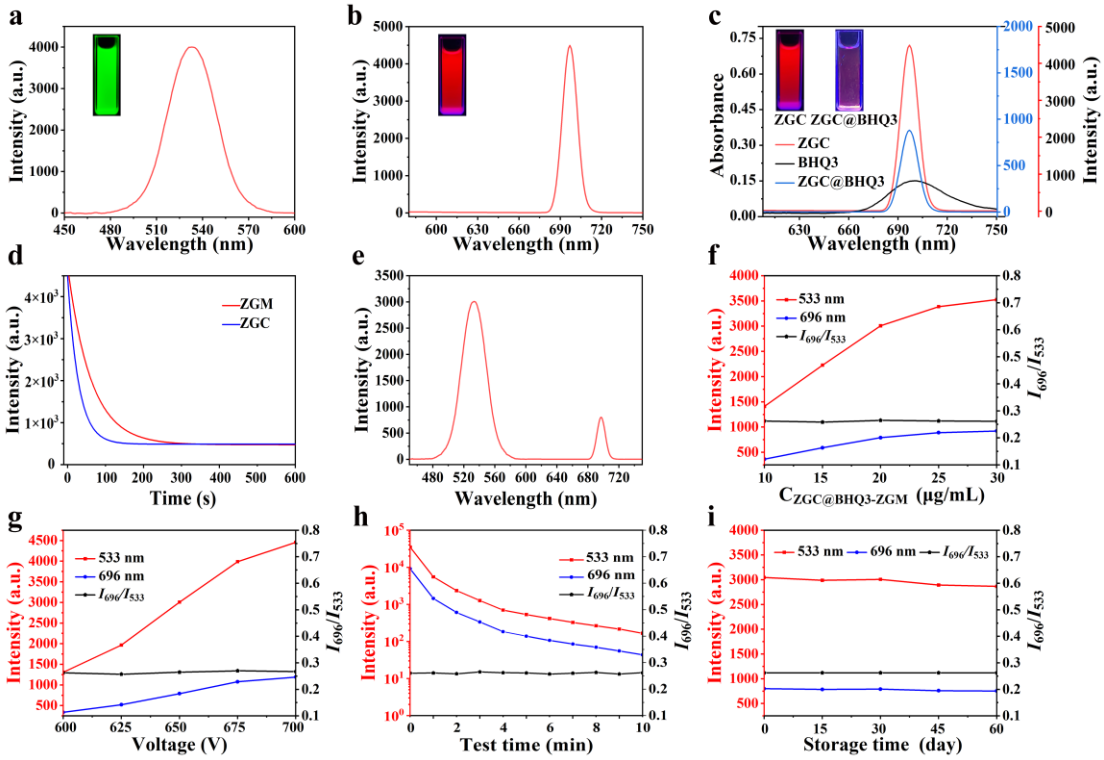

582

583 Figure 5

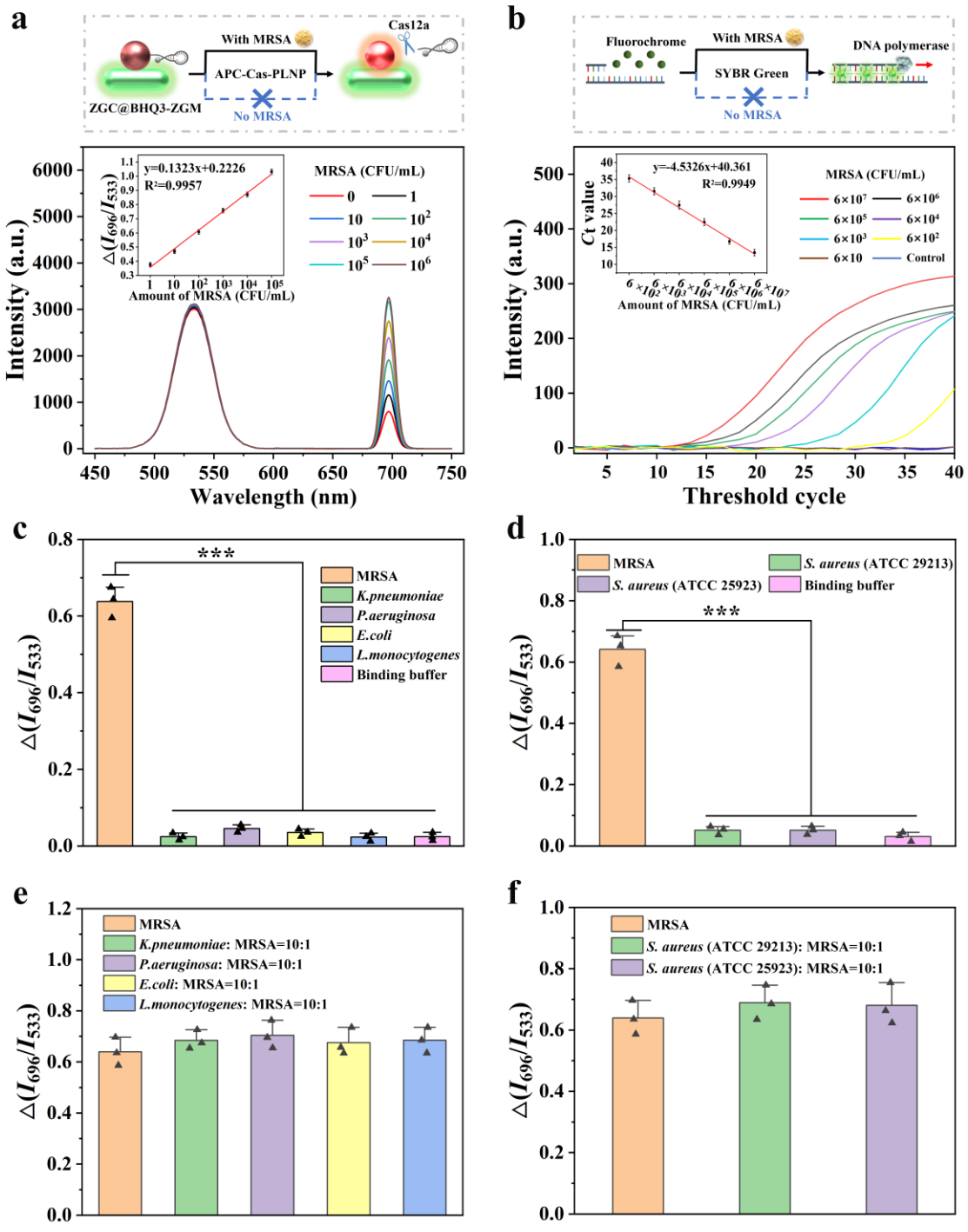

584

585 Figure 6

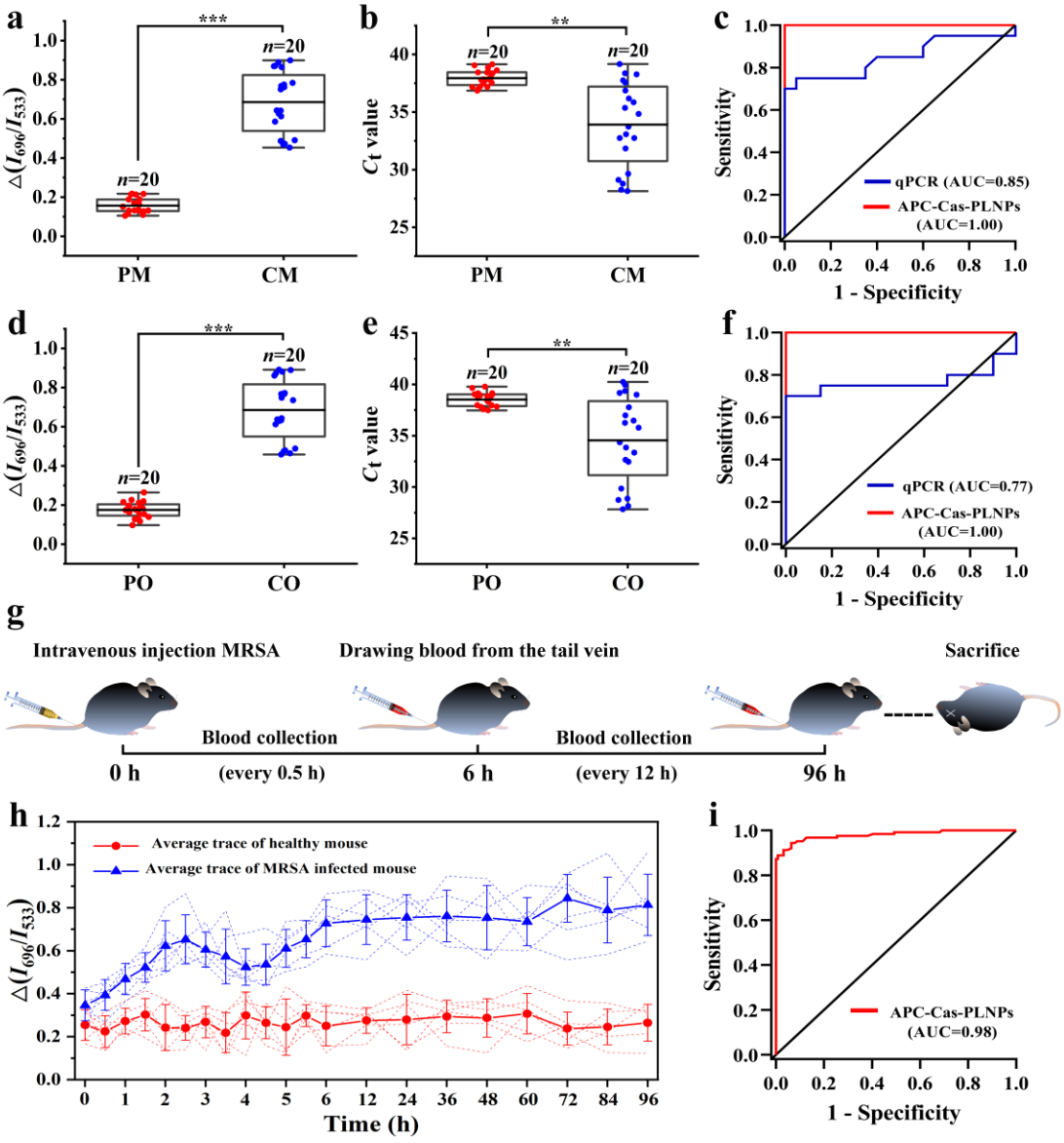

586